ARTICLE

Check for updates

Gold-in-copper at low *CO coverage enables efficient electromethanation of CO_2

Xue Wang [1,8], Pengfei Ou [1,8], Joshua Wicks [1,8], Yi Xie[2,8], Ying Wang [2,8], Jun Li [3], Jason Tam[4], Dan Ren [3], Jane Y. Howe[4], Ziyun Wang [1], Adnan Ozden[5], Y. Zou Finfrock[6,7], Yi Xu [5], Yuhang Li [1], Armin Sedighian Rasouli[1], Koen Bertens[1], Alexander H. Ip[1], Michael Graetzel [3], David Sinton [5] & Edward H. Sargent [1✉]

The renewable-electricity-powered CO_2 electroreduction reaction provides a promising means to store intermittent renewable energy in the form of valuable chemicals and dispatchable fuels. Renewable methane produced using CO_2 electroreduction attracts interest due to the established global distribution network; however, present-day efficiencies and activities remain below those required for practical application. Here we exploit the fact that the suppression of *CO dimerization and hydrogen evolution promotes methane selectivity: we reason that the introduction of Au in Cu favors *CO protonation vs. C−C coupling under low *CO coverage and weakens the *H adsorption energy of the surface, leading to a reduction in hydrogen evolution. We construct experimentally a suite of Au-Cu catalysts and control *CO availability by regulating CO_2 concentration and reaction rate. This strategy leads to a 1.6× improvement in the methane:H_2 selectivity ratio compared to the best prior reports operating above 100 mA cm^{-2}. We as a result achieve a CO_2-to-methane Faradaic efficiency (FE) of (56 ± 2)% at a production rate of (112 ± 4) mA cm^{-2}.

[1] Department of Electrical and Computer Engineering, University of Toronto, Toronto, ON, Canada. [2] Department of Chemistry, The Chinese University of Hong Kong, Hong Kong, S.A.R., China. [3] Institute of Chemical Sciences and Engineering, École Polytechnique Fédérale de Lausanne, Lausanne, Switzerland. [4] Department of Materials Science and Engineering, University of Toronto, Toronto, ON, Canada. [5] Department of Mechanical and Industrial Engineering, University of Toronto, Toronto, ON, Canada. [6] Science Division, Canadian Light Source, Saskatoon, SK, Canada. [7] Photon Science Division, Argonne National Laboratory, Lemont, IL, USA. [8]These authors contributed equally: Xue Wang, Pengfei Ou, Joshua Wicks, Yi Xie, Ying Wang. ✉email: ted.sargent@utoronto.ca

The CO$_2$ electroreduction reaction (CO$_2$RR) to valuable fuels and feedstocks, powered using renewable electricity, offers a sustainable approach to store intermittent renewable energy[1]. Prior CO$_2$RR studies have reported the generation of C$_1$ to C$_3$ chemicals such as CO, methane, formate, ethylene, ethanol, and n-propanol[2–10]. Among these products, carbon-neutral methane produced from CO$_2$RR is desired due to well-established natural gas infrastructure[11].

Practical CO$_2$RR systems need to produce a desired product with high selectivity, conversion rate, and energy efficiency (EE)[12,13]. In prior reports, most advances in improving the selectivity to methane in CO$_2$RR operate at current densities below 50 mA cm^{-2} (ref. [14–18]). Techno-economic analyses suggest that compelling CO$_2$RR systems require current densities above 100 mA cm^{-2} (ref. [19]), which prompted us to concentrate on improving the performance of CO$_2$RR to methane in high current density regimes (>100 mA cm^{-2}).

In CO$_2$RR, *CO protonation to *CHO is the potential-determining step for methane formation, and it competes with C–C coupling toward C$_2$ products[20,21]. In addition, *CO protonation competes with the hydrogen evolution reaction (HER), since both need *H (ref. [22]). The simultaneous suppression of both HER and C–C coupling will improve methane selectivity.

Early studies by Hori et al.[2] showed that Cu is the transition metal catalyst that generates methane and C$_{2+}$ products; but that it did so with low product selectivity. Introducing a second metal into Cu has been shown to be a promising route to tune the product selectivity in CO$_2$RR (refs. [23–30]). Prior studies report that Au–Cu bimetallic catalysts of varying structures exhibit good selectivity to CO or alcohols, albeit with pure CO$_2$ feeds (refs. [31–34]). Here we present a strategy wherein we regulate *CO availability on Au–Cu catalysts, enabling selectivity to methane at high production rates in CO$_2$RR. Density functional theory (DFT) calculations indicate that the introduction of Au in Cu not only steers the selectivity from C–C coupling to *CO protonation under low *CO coverage, but also tends to suppress HER relative to Cu. By implementing this concept experimentally, we achieve an FE of (56 ± 2)% to methane. The methane:H$_2$ selectivity ratio is improved 1.6× compared with prior reports having a total current density above 100 mA cm^{-2} (Supplementary Table 1) (refs. [35–39]).

Results

DFT calculations. In a previous study, we found that lowering the *CO coverage on a Cu surface improved the selectivity to methane in CO$_2$RR while still suffering from prominent HER (ref. [35]). Introducing a second element to Cu, such as Ag, has been shown to suppress HER (refs. [21,28]). Au—like Ag—has a greater free energy of hydrogen adsorption than Cu, suggesting that it is also a poor HER catalyst[40]. We thus use Au–Cu as a representative example to assess methane selectivity on catalysts with HER-suppressing dopants under different *CO coverages. In addition, we note that selecting an element that is on the same side of the hydrogen adsorption volcano curve as Cu avoids any synergistic effects that may optimize the *H binding energy leading to better HER, such as with Cu–Ni or Cu–Pt (refs. [41–43]).

Computationally, we built three Au–Cu surfaces by replacing one, two, or three surface Cu atoms of a (3 × 3 × 4) Cu(111) supercell with Au atoms, denoted Au$_1$Cu$_{35}$, Au$_2$Cu$_{34}$, and Au$_3$Cu$_{33}$, respectively. With DFT, we first calculated the reaction free energies of *CO to *CHO (ΔG_{*CHO}) for methane formation and C–C coupling (ΔG_{*OCCOH}) for C$_2$ products on these Au–Cu surfaces under different *CO coverages (Fig. 1a, Supplementary Figs. 1–4, and Supplementary Tables 2 and 3). ΔG_{*CHO}–ΔG_{*OCCOH} is used as a descriptor of the propensity for *CO protonation vs. C–C coupling. We found that the values of ΔG_{*CHO}–ΔG_{*OCCOH} on Au–Cu surfaces decrease when one reduces *CO coverage from 4/9 to 2/9 monolayer (ML) (Fig. 1b), a trend similar to that on Cu. Thus lowering *CO coverage on Au–Cu surfaces is predicted to favor methane vs. C$_2$ products, as previously shown on Cu (ref. [35]). In addition, DFT calculation results show that the values of ΔG_{*CHO}–ΔG_{*OCCOH} on Au–Cu surfaces are not always lower than the values of ΔG_{*CHO}–ΔG_{*OCCOH} on Cu at different *CO coverages (Fig. 1b), suggesting that only under low *CO coverage do some Au–Cu surfaces show a higher ratio of methane to C$_2$ products compared to Cu.
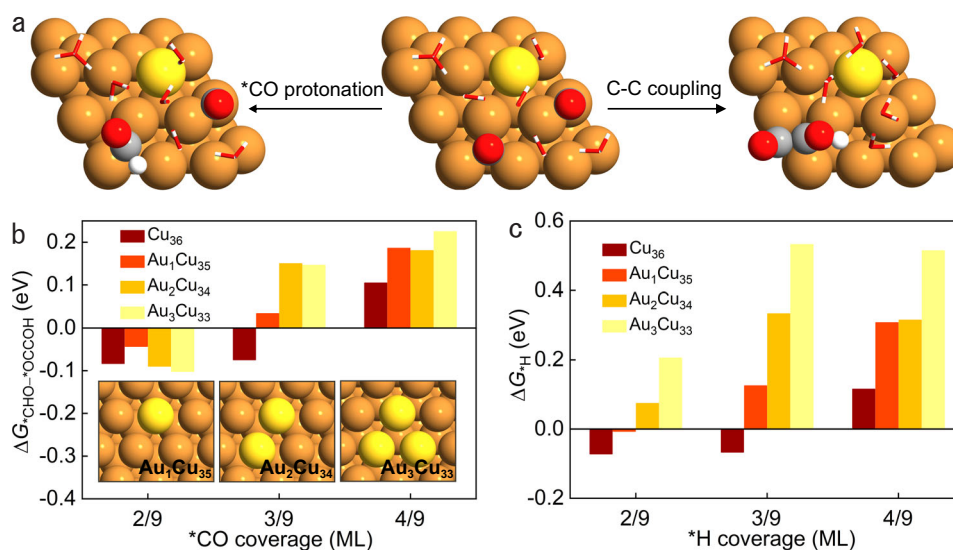
Fig. 1 DFT studies. a Geometries of *CO, *CHO, and *OCCOH intermediates on Au–Cu surface, showing the competitive steps of *CO protonation and C–C coupling. **b** Reaction free energy difference between *CO protonation and C–C coupling steps on Cu$_{36}$, Au$_1$Cu$_{35}$, Au$_2$Cu$_{34}$, and Au$_3$Cu$_{33}$ surfaces under varying *CO coverages. **c** Reaction free energies for *H intermediate formation under varying *H coverages on Cu$_{36}$, Au$_1$Cu$_{35}$, Au$_2$Cu$_{34}$, and Au$_3$Cu$_{33}$ surfaces. Cu, Au, C, O, and H atoms in Fig. 1 are illustrated as orange, yellow, grey, red, and white spheres, respectively, while the water molecules are shown as sticks. Source data are provided as a Source Data file.

To compare the HER activities on Cu and Au–Cu surfaces, we calculated the reaction free energies of *H intermediate formation (ΔG_{*H}) (Fig. 1c and Supplementary Fig. 5). The results suggest that Au–Cu surfaces tend to suppress HER compared to Cu under high *H coverages (Fig. 1c).

Taken together, these DFT studies suggest that Au–Cu tends to promote methane selectivity with low *CO coverage, since this will suppress C–C coupling; and that Au–Cu will further advance CO_2RR over HER compared to pure Cu.

Preparation and characterization of catalysts. To achieve the goal of high selectivity to methane in CO_2RR with high current densities, we sought to fabricate Au–Cu catalysts. We used a galvanic replacement approach enabled by the differing reduction potentials of Au and Cu (ref. [44]). Firstly, we prepared a 100 nm thick layer of Cu catalysts on the surface of polytetrafluoroethylene (PTFE) nanofibers via sputter deposition (Supplementary Figs. 6 and 7). We then immersed the Cu/PTFE in an N_2-saturated $HAuCl_4$ aqueous solution at 65 °C for 15 min to prepare the Au–Cu catalysts on PTFE as the electrodes (Fig. 2a–d) via the galvanic replacement between Cu and $AuCl_4^-$—this approach allows us to directly tune the ratio of Au and Cu on PTFE substrates.

Low-magnification scanning electron microscope (SEM) images and energy-dispersive X-ray spectroscopy (EDX) elemental mapping show a uniform distribution of elemental Cu and Au on PTFE nanofibers, accompanied by loosely distributed Au nanoparticles also on the nanofibers (Fig. 2a, b). The bright-field scanning transmission electron microscope (STEM) image with higher magnification and corresponding EDX elemental mapping further confirms that Au and Cu are distributed evenly on the PTFE nanofibers (Fig. 2d). High-resolution X-ray photoelectron spectroscopy (XPS) characterization of Au–Cu

electrodes shows the presence of Au^0 and Cu which has been partially oxidized to Cu^+ in the air (Fig. 2e, f and Supplementary Figs. 8 and 9)[45]. The atomic percentage of Au in the catalyst surface is approximately 7% determined by XPS (denoted 7% Au–Cu), which is lower than previously reported Au–Cu alloy catalysts studied in CO_2RR (refs. [31–33]).

Investigation of CO_2 electroreduction. The CO_2RR experiments were performed in a flow cell reactor with a three-electrode configuration (Supplementary Figs. 10 and 11) using CO_2-saturated 1 M $KHCO_3$ aqueous solution as the electrolyte. Previous studies show that, in CO_2RR, both reaction rate—determined by current density—and CO_2 concentration affect the concentration of *CO on the catalyst surface[35]. We thus evaluated the CO_2RR performance of 7% Au–Cu electrodes by supplying gas streams consisting of different volume ratios of CO_2 to N_2 (Fig. 3, Supplementary Figs. 12 and 13, and Supplementary Table 4).

Figure 3a, b shows FEs of methane and ethylene on 7% Au–Cu catalysts in the current density range of 100–250 mA cm^{-2} at various CO_2 concentrations (25% CO_2, 50% CO_2, 75% CO_2, 84% CO_2, 92% CO_2, and pure CO_2). At low current densities (≤150 mA cm^{-2}), 7% Au–Cu delivers appreciable ethylene FEs under pure CO_2 and CO_2–N_2 mixed streams (Fig. 3b). However, at high current densities (200–250 mA cm^{-2}), relative to pure CO_2, the methane FEs on 7% Au–Cu catalysts increase sharply in CO_2–N_2 mixed streams while the ethylene FEs decrease dramatically, which we ascribe to the low *CO coverage on catalyst surfaces as a result of the reduced CO_2 concentration and high reaction rate. We note that, once they reach their peaks in these mixed streams, the methane FEs start to decrease with further increase in current density (Fig. 3a), a finding we attribute to the lack of *CO for the *CO protonation step of methane formation[46]. In particular, at 84% CO_2, we achieve the highest CH_4 FE of
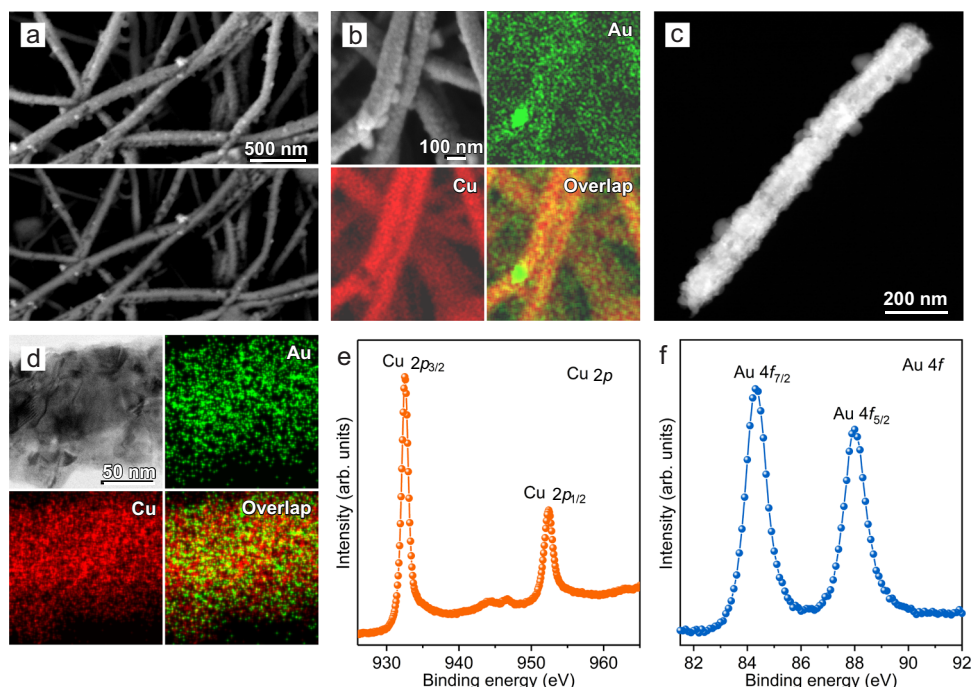

Fig. 2 Structural and compositional analyses of 7% Au-Cu catalysts on PTFE. a Low magnification secondary electron image (above) and the corresponding backscattered electron image (below) of the 7% Au-Cu/PTFE, showing the dispersed Au nanoparticles (bright spots). **b** Secondary electron image and the corresponding EDX elemental mapping of Au and Cu for the 7% Au-Cu/PTFE. **c** High-angle annular dark-field scanning transmission electron microscopy (HAADF-STEM) image of one 7% Au-Cu/PTFE nanofiber. **d** High-magnification bright-field STEM image and the corresponding elemental mapping of Au and Cu from a section of one 7% Au-Cu/PTFE nanofiber. **e, f** High-resolution XPS spectra of Cu 2p (**e**) and Au 4f (**f**) for 7% Au-Cu/PTFE.
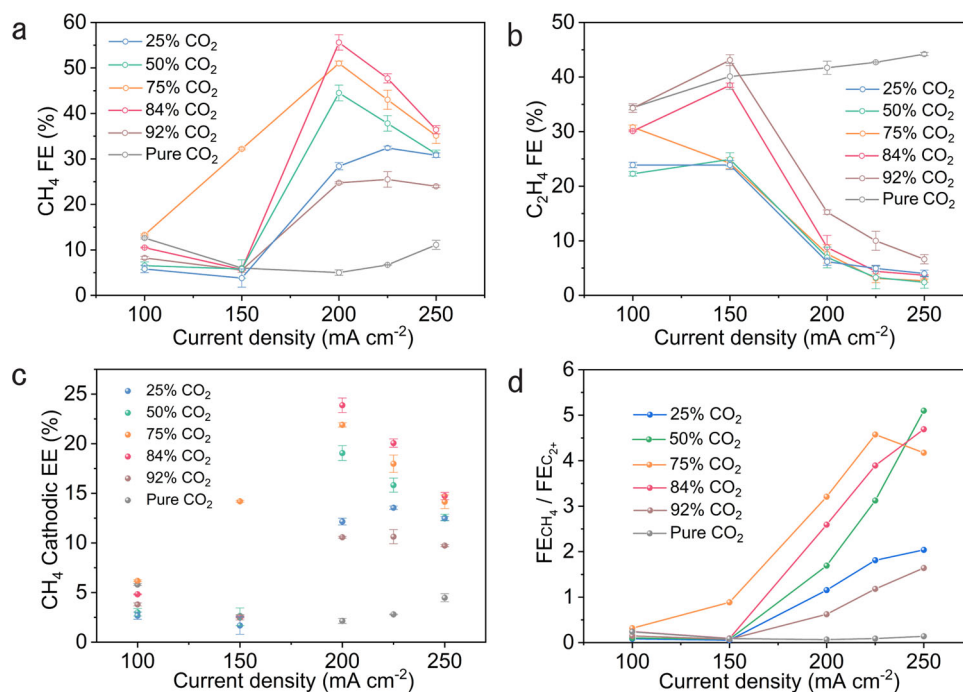
Fig. 3 CO₂RR performance of 7% Au–Cu catalysts at various CO₂ concentrations. a Methane FEs on 7% Au–Cu at various CO₂ concentrations. **b** Ethylene FEs on 7% Au–Cu at various CO₂ concentrations. **c** CH₄ cathodic EEs at different current densities under different CO₂ concentrations. **d** Comparison of $FE_{CH_4}/FE_{C_{2+}}$ ratios on 7% Au–Cu catalysts at various CO₂ concentrations. Error bars represent the standard deviation based on three separate measurements.

$(56 \pm 2)\%$ on 7% Au–Cu catalysts with a CH₄ production rate of (112 ± 4) mA cm⁻². We calculated the CH₄ cathodic EEs at different current densities under different CO₂ concentrations (Fig. 3c): the highest CH₄ cathodic EE of $(24 \pm 1)\%$ was achieved at 200 mA cm⁻² under 84% CO₂.

To evaluate experimentally the selectivity between *CO protonation and C−C coupling reaction steps, we further calculated the ratios of methane FE to total C₂₊ FE ($FE_{CH_4}/FE_{C_{2+}}$) on 7% Au–Cu catalysts at various CO₂ concentrations (Fig. 3d). With low reaction rates (≤150 mA cm⁻²), the C₂₊ selectivity is higher than the methane selectivity regardless of the CO₂ concentration. Under high current densities (200–250 mA cm⁻²), the $FE_{CH_4}/FE_{C_{2+}}$ ratio on 7% Au–Cu catalysts in CO₂–N₂ mixed streams is much greater than that in pure CO₂, suggesting that low *CO coverage on the surface of Au–Cu catalysts—as a consequence of a reduced CO₂ concentration and high current density—promotes the *CO protonation step for methane production, consistent with our DFT calculations.

To explore the effect of Au concentration on CO₂RR performance under CO₂–N₂ co-feeds, we also prepared 3% Au–Cu and 10% Au–Cu catalysts on PTFE through a similar galvanic replacement approach (Supplementary Figs. 7 and 14–19) and measured CO₂RR performance of the 3% Au–Cu, 10% Au–Cu, and Cu catalysts at 84% CO₂ for comparison (Fig. 4a–c, Supplementary Figs. 20 and 21, and Supplementary Table 5). At low reaction rates (≤150 mA cm⁻²), the methane FEs on 3% Au–Cu, 7% Au–Cu, 10% Au–Cu, and Cu catalysts are below 11% (Fig. 4a), while ethylene and ethanol are the main CO₂RR products on these catalysts (Supplementary Fig. 20c and Supplementary Table 5). At high reaction rates (200–250 mA cm⁻²), methane becomes the main CO₂RR product while ethylene FEs are below 12% on the 3% Au–Cu, 10% Au–Cu, and Cu catalysts; methane FEs on 3% Au–Cu, 10% Au–Cu, and Cu catalysts give peak values at 200 mA cm⁻² and then decrease along with the increase in current density (Fig. 4a). These trends are similar to that observed on the 7% Au–Cu

catalysts. By comparing the highest methane FEs on different catalysts, we note that, among the catalysts studied, only 7% Au–Cu catalysts deliver higher methane FE vs. Cu catalysts (Fig. 4b), suggesting the significance of controlling Au concentration in Au–Cu catalysts for promoting methane selectivity. The 7% Au–Cu delivers—compared to 3% Au–Cu and 10% Au–Cu—higher methane FE at 200 mA cm⁻². We associate this with improved suppression of HER on 7% Au–Cu (Supplementary Fig. 20a) and note that both HER and *CO coverage impact methane FE. We also calculated the $FE_{CH_4}/FE_{C_{2+}}$ ratios on Cu and three Au–Cu catalysts at 84% CO₂: only at high current density—low *CO coverage—do some of Au–Cu catalysts show higher $FE_{CH_4}/FE_{C_{2+}}$ ratios compared to Cu, in agreement with DFT calculations.

At high current densities (200–250 mA cm⁻²) with high methane selectivity, the H₂ FEs on 3% Au–Cu, 7% Au–Cu, and 10% Au–Cu catalysts are lower than that on the Cu catalysts (Supplementary Fig. 20a), suggesting that the introduction of Au in Cu tends to suppress HER when using dilute CO₂ feeds. We further calculated the ratio of methane FE to H₂ FE (FE_{CH_4}/FE_{H_2}) on catalysts in high current density regimes (Fig. 4c): compared with Cu catalysts, 3% Au–Cu, 7% Au–Cu, and 10% Au–Cu catalysts exhibit higher FE_{CH_4}/FE_{H_2} ratios—with the highest value of 2.7 on 7% Au–Cu catalysts— indicating that the Au–Cu catalysts shifted the reaction from undesired HER toward *CO protonation for methane production.

To investigate the chemical state of Cu in the catalysts during CO₂RR, we carried out operando X-ray absorption spectroscopy (XAS) at the Cu K-edge at a constant current density of 200 mA cm⁻² with an 84% CO₂ feed (Fig. 4d). The average valence states of Cu in 3% Au–Cu, 7% Au–Cu, 10% Au–Cu, and Cu catalysts are zero during CO₂RR, demonstrating that the difference in product selectivity among these catalysts is associated with the metallic state of Cu in lieu of copper oxides[5,47].
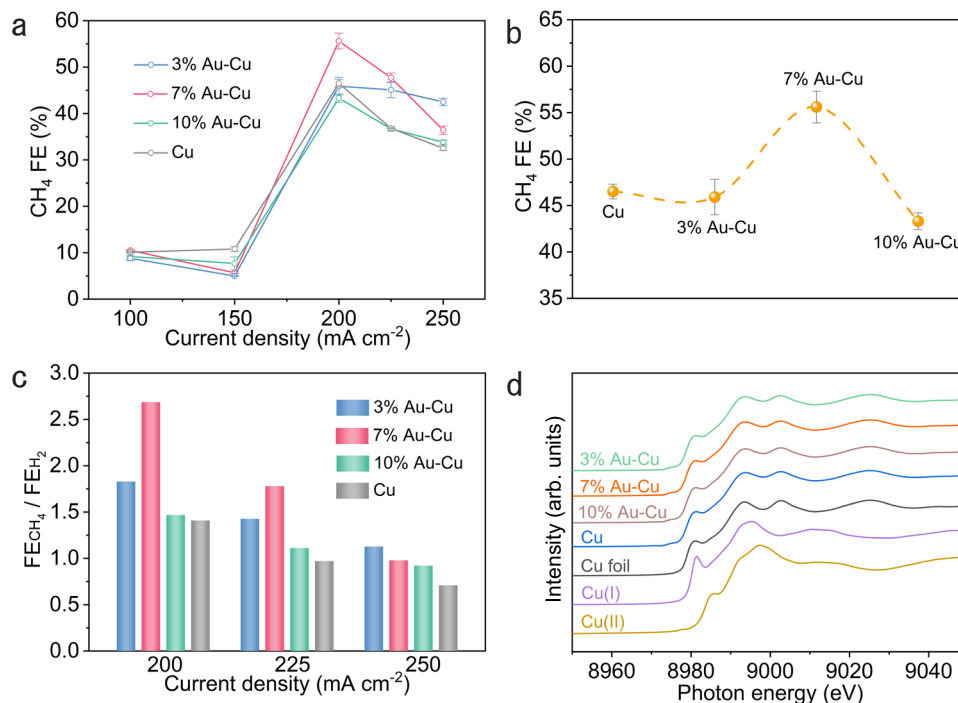
Fig. 4 CO₂RR performance at 84% CO₂ and operando XAS characterization. a Methane FEs on different catalysts at 84% CO₂. **b** Comparison of methane FEs on different catalysts at 200 mA cm⁻². Error bars represent the standard deviation based on three separate measurements. **c** Comparison of $FE_{CH_4}/FE_{H_{2+}}$ ratios on different catalysts at 84% CO₂. **d** Operando Cu K-edge XANES spectra of different catalysts during CO₂RR with a constant current density of 200 mA cm⁻². Bulk Cu foil, Cu₂O, and CuO are listed as references.
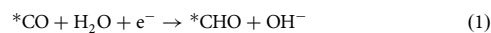
Discussion

This work demonstrates that the introduction of Au in Cu facilitates *CO protonation for methane formation using CO₂–N₂ co-feeds and suppresses HER at high current densities. DFT results show that a decrease in *CO coverage on Au–Cu surfaces favors *CO protonation vs. C–C coupling; compared with Cu, Au–Cu suppresses HER, enabling methane selectivity improvements under dilute CO₂ streams. Experimentally, we fabricated Au–Cu catalysts and regulated *CO availability by controlling the CO₂ concentration and current density, wherein the selectivity ratio of methane to H₂ exhibited the highest value of 2.7. We report a CO₂-to-methane conversion with a high methane FE of (56 ± 2)% at a partial current density of (112 ± 4) mA cm⁻² with a CO₂–N₂ co-feed. These findings suggest a promising strategy to convert CO₂ to carbon-neutral methane with a combination of high selectivity, high conversion rate, and high cathodic EE through catalyst design and tuning local *CO coverage.

Methods

DFT calculations. In the Vienna ab initio simulation package, the generalized gradient approximation and the Perdew–Burke–Ernzerhof exchange-correlation functional was implemented for all DFT calculations[48–52]. The projector-augmented wave (PAW) method was used to treat the electron–ion interactions[53,54] with an energy cut-off of 450 eV for the plane-wave basis set. The force and energy convergence for all DFT calculations were set to 0.01 eV Å⁻¹ and 10⁻⁵ eV, respectively. A (3 × 3 × 4) Cu(111) supercell with the bottom two layers fixed was used to simulate the exposed Cu surface with a 15 Å vacuum gap. One, two, or three surface Cu atoms were substituted by Au atoms in the Au₁Cu₃₅, Au₂Cu₃₄, and Au₃Cu₃₃, respectively. A (3 × 3 × 1) Monkhorst–Pack k-points grid was used to optimize all the surface structures. In DFT calculations, we did not consider the isolated arrangement of Au dopants in Cu as the XAS characterization of the Au–Cu catalysts showed that Au atoms were not atomically dispersed in Cu (Supplementary Fig. 22 and Supplementary Table 6).

Surface *CO coverages of 2/9 ML, 3/9 ML, and 4/9 ML were studied, where 2/9 ML corresponds to two single-carbon adsorbed species or one double-carbon species on the surface of the supercell. To systematically determine the most stable geometry of each reaction intermediate in CO₂RR and HER under different *CO coverages (2/9, 3/9, and 4/9 ML) on different surfaces (Cu₃₆, Au₁Cu₃₅, Au₂Cu₃₄, and Au₃Cu₃₃), we considered

different possibilities of *CO adsorption, protonation, and C–C coupling, as well as different directions of *OCCO protonation (more details of our computational workflow in Supplementary Fig. 23). We note that the models reported in this study include a charged water layer, i.e., an ML of six water molecules, one of which is a hydronium or charged water (H₃O⁺) molecule, to consider both field and solvation effects[55]. The water structure was determined by ab initio molecular dynamics and adopted from a previous study[56]. The two competing CO₂RR reaction steps as listed below[57–61] were simulated for the three *CO coverages while *H adsorption was simulated for equivalent *H coverages

$$*CO + H_2O + e^- \rightarrow *CHO + OH^- \tag{1}$$

$$*CO + *CO + H_2O + e^- \rightarrow *OCCOH + OH^- \tag{2}$$

$$H^+ + e^- + * \rightarrow *H \tag{3}$$

The Gibbs free energy changes (ΔG) for *CO protonation, C–C coupling, and *H adsorption were calculated without dipole corrections based on the computational hydrogen electrode (CHE) model[62]. The Gibbs free energy of adsorbed and non-adsorbed species (G) is calculated as

$$G = E + ZPE + \int Cp dT - TS \tag{4}$$

where E, ZPE, Cp, and S are the electronic energy directly obtained from DFT calculations, zero-point energy, heat capacity, and entropy, respectively (see Supplementary Table 2 for more details). T is set to room temperature (298.15 K) for a better comparison with the experimental measurements.

Electrode preparation. All chemicals were used as received without further purification. All aqueous solutions were prepared using deionized water with a resistivity of 18.2 MΩ cm. The Cu/PTFE cathodes were prepared by sputtering 100 nm thickness of Cu catalysts (Cu target, 99.999%, Kurt J. Lesker company) on PTFE membranes (pore size: 450 nm, Beijing Zhongxingweiye Instrument Co., Ltd.) using a magnetron sputtering system. In the cathode, a porous PTFE membrane functions as a stable hydrophobic gas diffusion layer and prevents flooding during operation[7]. 3% Au–Cu, 7% Au–Cu, and 10% Au–Cu cathodes were prepared by immersing the Cu/PTFE electrodes in N₂-saturated HAuCl₄ aqueous solution (5 μmol L⁻¹) at 40 °C for 30 min, 65 °C for 15 min, and 65 °C for 30 min, respectively. Ag/AgCl reference electrode (3 M KCl, BASi) and Ni foam (1.6 mm thickness, MTI Corporation) was used as the reference electrode and anode, respectively. Ni foam was used as an OER electrode in the anode due to its commercial availability and good stability[35,63].

Material characterization. SEM images and the corresponding EDX elemental mapping were taken using the Hitachi FE-SEM SU5000 microscope. HAADF-

STEM and bright-field STEM images, and the corresponding EDX elemental mapping were taken using a Hitachi HF-3300 microscope at 300 kV. XRD was recorded on Rigaku SmartLab X-ray diffractometer with Cu-Kα radiation. The surface compositions of electrodes were determined by XPS (Thermo Scientific K-Alpha) using a monochromatic aluminum X-ray source. Operando Cu K-edge XAS spectra recorded in fluorescence yield were performed at the SuperXAS beamline at the Swiss Light Source. Ex situ XAS measurements were carried out at the Advanced Photon Source (Argonne National Laboratory). XAS data were processed by Athena and Artemis software included in a standard IFEFFIT package[64].

Electrochemical measurements. The electrochemical measurements were conducted in an electrochemical flow cell setup configuration with the three-electrode system at an electrochemical station (AUT50783). The geometric area of the cathode in the flow cell is 1 cm^2, which is used for all current density calculations. 30 mL of CO_2-saturated 1 M $KHCO_3$ aqueous solution was introduced into the cathode chamber and the anode chamber at the rate of 10 mL min^{-1} by two pumps, respectively. An anion exchange membrane (Fumasep FAB-PK-130, Fuel Cell Store) was used to separate the cathode chamber and anode chamber. Pure CO_2 gas (Linde, 99.99%) or N_2-diluted CO_2 gas with different CO_2 concentrations (75% and 84%) was continuously supplied to the gas chamber of the flow cell at a flow rate of 90 mL min^{-1}. The CO_2RR performance was tested using constant-current electrolysis while purging CO_2 into the catholyte during the whole electrochemical test. The potentials vs. Ag/AgCl reference electrode were converted to values vs. reversible hydrogen electrode using the equation

$$E_{RHE} = E_{Ag/AgCl} + 0.210\,V + 0.0591 \times pH \qquad (5)$$

The ohmic loss between the working and reference electrodes was evaluated by electrochemical impedance spectroscopy technique and 80% iR compensation was applied to correct the potentials manually.

Gas products were analyzed using a gas chromatograph (PerkinElmer Clarus 600) equipped with thermal conductivity and flame ionization detectors. Liquid products were analyzed by nuclear magnetic resonance spectrometer (Agilent DD2 600 MHz) and dimethylsulfoxide was used as an internal standard.

We calculated the methane cathodic EE based on the equation as follows[7]:

$$Cathodic\,EE = \frac{(1.23 + (-E_{methane})) \times FE_{methane}}{(1.23 + (-E_{applied}))}, \qquad (6)$$

where the overpotential of oxygen evolution is assumed to be 0, $E_{applied}$ is the potential used in the experiment, $FE_{methane}$ is the measured Faradaic efficiency of methane in percentage, and $E_{methane} = 0.17\,V_{RHE}$ for CO_2RR (ref. [65]).

Data availability

The data supporting this study are available within the paper and the Supplementary Information. The source data of the geometries optimized by DFT calculations are provided in this paper. Source data are provided with this paper.

References

1. Jhong, H.-R., Ma, S. & Kenis, P. J. A. Electrochemical conversion of CO_2 to useful chemicals: current status, remaining challenges, and future opportunities. *Curr. Opin. Chem. Eng.* **2**, 191–199 (2013).
2. Hori, Y. "Electrochemical CO_2 Reduction on Metal Electrodes". In *Modern Aspects of Electrochemistry No. 42.* (eds Vayenas, C. G., White, R. E. & Gamboa-Aldeco, M. E.) (Springer, 2008) Chapter 3.
3. Qiao, J., Liu, Y., Hong, F. & Zhang, J. A review of catalysts for the electroreduction of carbon dioxide to produce low-carbon fuels. *Chem. Soc. Rev.* **43**, 631–675 (2014).
4. Kim, D., Kley, C. S., Li, Y. & Yang, P. Copper nanoparticle ensembles for selective electroreduction of CO_2 to C_2–C_3 products. *Proc. Natl Acad. Sci. USA* **114**, 10560–10565 (2017).
5. Zhou, Y. et al. Dopant-induced electron localization drives CO_2 reduction to C_2 hydrocarbons. *Nat. Chem.* **19**, 974–980 (2018).
6. Ren, R. et al. Molecular electrocatalysts can mediate fast, selective CO_2 reduction in a flow cell. *Science* **365**, 367–369 (2019).
7. Dinh, C.-T. et al. CO_2 electroreduction to ethylene via hydroxide-mediated copper catalysis at an abrupt interface. *Science* **360**, 783–787 (2018).
8. Xia, C. et al. Continuous production of pure liquid fuel solutions via electrocatalytic CO_2 reduction using solid-electrolyte devices. *Nat. Energy* **4**, 776–785 (2019).
9. Li, F. et al. Cooperative CO_2-to-ethanol conversion via enriched intermediates at molecule–metal catalyst interfaces. *Nat. Catal.* **3**, 75–82 (2020).
10. Wang, X. et al. Efficient electrically powered CO_2-to-ethanol via suppression of deoxygenation. *Nat. Energy* **5**, 478–486 (2020).
11. Howarth, R. W. & Ingraffea, A. Should fracking stop? *Nature* **477**, 271–275 (2011).
12. Ren, S. et al. Molecular electrocatalysts can mediate fast, selective CO_2 reduction in a flow cell. *Science* **365**, 367–369 (2019).
13. García de Arquer, F. P. et al. CO_2 electrolysis to multicarbon products at activities greater than 1 A cm^{-2}. *Science* **367**, 661–666 (2020).
14. Qiu, Y.-L. et al. Copper electrode fabricated via pulse electrodeposition: toward high methane selectivity and activity for CO_2 electroreduction. *ACS Catal.* **7**, 6302–6310 (2017).
15. Manthiram, K., Beberwyck, B. J. & Alivisatos, A. P. Enhanced electrochemical methanation of carbon dioxide with a dispersible nanoscale copper catalyst. *J. Am. Chem. Soc.* **136**, 13319–13325 (2014).
16. Li, Y. et al. Structure-sensitive CO_2 electroreduction to hydrocarbons on ultrathin 5-fold twinned copper nanowires. *Nano Lett.* **17**, 1312–1317 (2017).
17. Reske, R., Mistry, H., Behafarid, F., Cuenya, B. R. & Strasser, P. Particle size effects in the catalytic electroreduction of CO_2 on Cu nanoparticles. *J. Am. Chem. Soc.* **136**, 6978–6986 (2014).
18. Zhao, H. et al. Computational and experimental demonstrations of one-pot tandem catalysis for electrochemical carbon dioxide reduction to methane. *Nat. Commun.* **10**, 3340 (2019).
19. Jouny, M., Luc, W. & Jiao, F. General techno-economic analysis of CO_2 electrolysis systems. *Ind. Eng. Chem. Res.* **57**, 2165–2177 (2018).
20. Peterson, A. A., Abild-Pedersen, F., Studt, F., Rossmeisl, J. & Norskov, J. K. How copper catalyzes the electroreduction of carbon dioxide into hydrocarbon fuels. *Energy Environ. Sci.* **3**, 1311–1315 (2010).
21. Cheng, T., Xiao, H. & Goddard, W. A. Free-energy barriers and reaction mechanisms for the electrochemical reduction of CO on the Cu(100) surface, including multiple layers of explicit solvent at pH 0. *J. Phys. Chem. Lett.* **6**, 4767–4773 (2015).
22. Gattrel, M., Gupta, N. & Co, A. A review of the aqueous electrochemical reduction of CO_2 to hydrocarbons at copper. *J. Electroanal. Chem.* **594**, 1–19 (2006).
23. Hori, Y., Murata, A., Ito, S.-Y., Yoshinami, Y. & Koga, O. Nickel and iron modified copper electrode for electroreduction of CO_2 by in-situ electrodeposition. *Chem. Lett.* **18**, 1567–1570 (1989).
24. Watanabe, M., Shibata, M., Kato, A., Azuma, M. & Sakata, T. Design of alloy electrocatalysts for CO_2 reduction: III. The selective and reversible reduction of CO_2 on Cu alloy electrodes. *J. Electrochem. Soc.* **138**, 3382–3389 (1991).
25. Ren, D., Ang, B. & Yeo, B. Tuning the selectivity of carbon dioxide electroreduction toward ethanol on oxide-derived Cu_xZn catalysts. *ACS Catal.* **6**, 8239–8247 (2016).
26. Varela, A. S. et al. CO_2 electroreduction on well-defined bimetallic surfaces: Cu overlayers on Pt(111) and Pt(211). *J. Phys. Chem. C* **117**, 20500–20508 (2013).
27. Chen, C. S., Wan, J. H. & Yeo, B. S. Electrochemical reduction of carbon dioxide to ethane using nanostructured Cu_2O-derived copper catalyst and palladium(II) chloride. *J. Phys. Chem. C* **119**, 26875–26882 (2015).
28. Clark, E. L., Hahn, C., Jaramillo, T. F. & Bell, A. T. Electrochemical CO_2 reduction over compressively strained CuAg surface alloys with enhanced multi-carbon oxygenate selectivity. *J. Am. Chem. Soc.* **139**, 15848–15857 (2017).
29. Hoang, T. T. H. et al. Nanoporous Copper-silver alloys by additive-controlled electrodeposition for the selective electroreduction of CO_2 to ethylene and ethanol. *J. Am. Chem. Soc.* **140**, 5791–5797 (2018).
30. Zhong, M. et al. Accelerated discovery of CO_2 electrocatalysts using active machine learning. *Nature* **581**, 178–183 (2020).
31. Kim, D., Resasco, J., Yu, Y., Asiri, A. M. & Yang, P. Synergistic geometric and electronic effects for electrochemical reduction of carbon dioxide using gold-copper bimetallic nanoparticles. *Nat. Commun.* **5**, 4948 (2014).
32. Kim, D. et al. Electrochemical activation of CO_2 through atomic ordering transformations of AuCu nanoparticles. *J. Am. Chem. Soc.* **139**, 8329–8336 (2017).
33. Xu, Z., Lai, E., Shao-Horn, Y. & Hamad-Schifferli, K. Compositional dependence of the stability of AuCu alloy nanoparticles. *Chem. Commun.* **48**, 5626–5628 (2012).
34. Morales-Guio, C. G. et al. Improved CO_2 reduction activity towards C_{2+} alcohols on a tandem gold on copper electrocatalyst. *Nat. Catal.* **1**, 764–771 (2018).
35. Wang, X. et al. Efficient methane electrosynthesis enabled by tuning local CO_2 availability. *J. Am. Chem. Soc.* **142**, 3525–3531 (2020).
36. Zhuang, T.-T. et al. Steering post-C–C coupling selectivity enables high efficiency electroreduction of carbon dioxide to multi-carbon alcohols. *Nat. Catal.* **1**, 421–428 (2018).
37. Ma, S. et al. Electroreduction of carbon dioxide to hydrocarbons using bimetallic Cu–Pd catalysts with different mixing patterns. *J. Am. Chem. Soc.* **139**, 47–50 (2017).

38. Jiang, K. et al. Metal ion cycling of Cu foil for selective C–C coupling in electrochemical CO_2 reduction. *Nat. Catal.* **1**, 111–119 (2018).

39. Li, Y. C. et al. Binding site diversity promotes CO_2 electroreduction to ethanol. *J. Am. Chem. Soc.* **141**, 8584–8591 (2019).

40. Nørskov, J. K. et al. Trends in the exchange current for hydrogen evolution. *J. Electrochem. Soc.* **152**, J23–J26 (2005).

41. Shen, Y. et al. Nickel–copper alloy encapsulated in graphitic carbon shells as electrocatalysts for hydrogen evolution reaction. *Adv. Energy Mater.* **8**, 1701759 (2018).

42. Sun, Q., Dong, Y., Wang, Z., Yin, S. & Zhao, C. Synergistic nanotubular copper-doped nickel catalysts for hydrogen evolution reactions. *Small* **14**, 1704137 (2018).

43. Chao, T. et al. Atomically dispersed copper–platinum dual sites alloyed with palladium nanorings catalyze the hydrogen evolution reaction. *Angew. Chem. Int. Ed.* **56**, 16047–16051 (2017).

44. Cobley, C. M. & Xia, Y. Engineering the properties of metal nanostructures via galvanic replacement reactions. *Mater. Sci. Eng. R Rep.* **70**, 44–62 (2010).

45. Platzman, I., Brener, R., Haick, H. & Tannenbaum, R. Oxidation of polycrystalline copper thin films at ambient conditions. *J. Phys. Chem. C* **112**, 1101–1108 (2008).

46. Li, C. W., Ciston, J. & Kanan, M. W. Electroreduction of carbon monoxide to liquid fuel on oxide-derived nanocrystalline copper. *Nature* **508**, 504–507 (2014).

47. Xiao, H., Goddard, W. A., Cheng, T. & Liu, Y. Cu metal embedded in oxidized matrix catalyst to promote CO_2 activation and CO dimerization for electrochemical reduction of CO_2. *Proc. Natl Acad. Sci. USA* **114**, 6685–6688 (2017).

48. Kresse, G. & Hafner, J. Ab initio molecular dynamics for liquid metals. *Phys. Rev. B* **47**, 558–561 (1993).

49. Kresse, G. & Hafner, J. Ab initio molecular-dynamics simulation of the liquid-metal–amorphous-semiconductor transition in germanium. *Phys. Rev. B* **49**, 14251–14269 (1994).

50. Kresse, G. & Furthmüller, J. Efficient iterative schemes for ab initio total-energy calculations using a plane-wave basis set. *Phys. Rev. B* **54**, 11169–11186 (1996).

51. Kresse, G. & Furthmüller, J. Efficiency of ab-initio total energy calculations for metals and semiconductors using a plane-wave basis set. *Comput. Mater. Sci.* **6**, 15–50 (1996).

52. Perdew, J. P., Burke, K. & Ernzerhof, M. Generalized gradient approximation made simple. *Phys. Rev. Lett.* **77**, 3865–3868 (1996).

53. Blöchl, P. E. Projector augmented-wave method. *Phys. Rev. B* **50**, 17953–17979 (1994).

54. Kresse, G. & Joubert, D. From ultrasoft pseudopotentials to the projector augmented-wave method. *Phys. Rev. B* **59**, 1758–1775 (1999).

55. Montoya, J. H., Shi, C., Chan, K. & Nørskov, J. K. Theoretical insights into a CO dimerization mechanism in CO_2 electroreduction. *J. Phys. Chem. Lett.* **6**, 2032–2037 (2015).

56. Wang, X. et al. Efficient upgrading of CO to C_3 fuel using asymmetric C-C coupling active sites. *Nat. Commun.* **10**, 5186 (2019).

57. Kortlever, R., Shen, J., Schouten, K. J. P., Calle-Vallejo, F. & Koper, M. T. M. Catalysts and reaction pathways for the electrochemical reduction of carbon dioxide. *J. Phys. Chem. Lett.* **6**, 4073–4082 (2015).

58. Liu, X. et al. pH effects on the electrochemical reduction of CO($_2$) towards C_2 products on stepped copper. *Nat. Commun.* **10**, 32 (2019).

59. Cheng, T., Xiao, H. & Goddard, W. A. Reaction mechanisms for the electrochemical reduction of CO_2 to CO and formate on the Cu(100) surface at 298 K from quantum mechanics free energy calculations with explicit water. *J. Am. Chem. Soc.* **138**, 13802–13805 (2016).

60. Cheng, T., Xiao, H. & Goddard, W. A. Full atomistic reaction mechanism with kinetics for CO reduction on Cu(100) from ab initio molecular dynamics free-energy calculations at 298 K. *Proc. Natl Acad. Sci. USA* **114**, 1795–1800 (2017).

61. Xiao, H., Cheng, T. & Goddard, W. A. Atomistic mechanisms underlying selectivities in C_1 and C_2 products from electrochemical reduction of CO on Cu(111). *J. Am. Chem. Soc.* **139**, 130–136 (2017).

62. Nørskov, J. K. et al. Origin of the overpotential for oxygen reduction at a fuel-cell cathode. *J. Phys. Chem. B* **108**, 17886–17892 (2004).

63. Zhu, W., Zhang, R., Qu, F., Asiri, A. M. & Sun, X. Design and application of foams for electrocatalysis. *Chemcatchem* **9**, 1721–1743 (2017).

64. Ravel, B. & Newville, M. ATHENA, ARTEMIS, HEPHAESTUS: data analysis for X-ray absorption spectroscopy using IFEFFIT. *J. Synchrotron Radiat.* **12**, 537–541 (2005).

65. Kuhl, K. P., Cave, E. R., Abram, D. N. & Jaramillo, T. F. New insights into the electrochemical reduction of carbon dioxide on metallic copper surfaces. *Energy Environ. Sci.* **5**, 7050–7059 (2012).

Acknowledgements

Author contributions

E.H.S. supervised the project. X.W. and E.H.S. conceived the idea. X.W. designed and carried out most of the experiments. P.O. and J.W. carried out DFT calculations. Y.X. and Y.W. carried out part of the electrochemical measurements and XRD. J.L., D.R., Y.Z.F. and M.G. contributed synchrotron X-ray spectroscopy measurements and analysis. J.T. and J.Y.H. performed the SEM and TEM characterizations. J.W., A.S.R. and K.B. carried out XPS measurements. Z.W., A.O., Y.X., Y.L., A.H.I. and D.S. assisted with the discussions. All authors discussed the results and contributed to the preparation of the paper.

Competing interests

The authors declare no competing interests.

Additional information

Supplementary information The online version contains supplementary material available at https://doi.org/10.1038/s41467-021-23699-4.

Correspondence and requests for materials should be addressed to E.H.S.

Peer review information *Nature Communications* thanks Sandra Hernandez-Aldave and other, anonymous, reviewers for their contributions to the peer review of this work.

Reprints and permission information is available at http://www.nature.com/reprints

Publisher's note Springer Nature remains neutral with regard to jurisdictional claims in published maps and institutional affiliations.